Compact Quad-Mode Planar Phased Array with Wideband for 5G Mobile Terminals

Syrytsin, Igor A.; Zhang, Shuai; Pedersen, Gert F.; Morris, Art

Compact Quad-Mode Planar Phased Array with Wideband for 5G Mobile Terminals

Igor Syrytsin, Shuai Zhang, Gert Frølund Pedersen, *Senior Member IEEE*, and Art Morris, *Fellow, IEEE*

Abstract—In this paper a quad-mode endfire planar phased antenna array with wide scan angle and 1.2 mm clearance is proposed for 5G mobile terminals. The proposed antenna can obtain over 8 GHz of impedance bandwidth. Here is suggested to efficiently combine a multi-mode array element with different radiation patterns for each mode into a phased antenna array. In the array, similar and wide embedded radiation patterns are obtained for the all four modes. Furthermore, a coaxial to differential stripline transition is designed in this work. The differential feeding structure is very compact and utilizes only MMPX connector and vias. The total scan pattern and coverage efficiency of the measured and simulated phased array antenna are calculated in the range from 25 to 33 GHz, and a good agreement between measured and simulated results is observed. The mean coverage efficiency along the frequency range is very similar, but minor difference in variance of coverage efficiency is observed in the measurements. The coverage efficiency of around 50 % for the threshold gain of 5 dBi is achieved in the chosen frequency range.

Index Terms—Antennas, mobile handset antenna, radiation pattern, coverage efficiency, total scan pattern, 5G antenna, planar antenna, wideband antenna, 5G phased array.

I. INTRODUCTION

IN the past few years, interests in the centimeter (cm) and millimeter (mm)-wave bands have grown [1]. In order to achieve communication speeds in GB/s the 28 GHz band has already been allocated by FCC for the future cellular communication systems. At the cm and mm-wave frequencies, higher free space path loss becomes a bigger design consideration for the link budgets. However, by using the directional high gain antennas the path loss can be compensated [2]. Furthermore, directional antennas can reduce doppler shift spread [3], reduce delay spread in wideband communication channels [4], and decrease the path loss exponent [5]. However, in the cellular communication systems the user mobility, urban indoor and outdoor propagation environments, and arbitrary mobile device orientation are some of the most important factors affecting the design of base and mobile station antennas. Thus, the beam steering should be implemented both at mobile and base stations to obtain the good link quality.

In order to verify the performance of the mobile device considering the arbitrary user equipment orientation the coverage efficiency metric has been proposed in [6]. This metric is

especially useful in the characterization of the mobile phased antenna array's performance [7]. Multi-polarized antenna array configuration for mmWave 5G mobile terminals has been proposed in [8]. A low-profile beam steering antenna solution for future 5G cellular applications has been designed and analyzed in [9]. A Vivaldi phased antenna array has been studied with the user in [10]. Compact 4G MIMO antenna integrated with a 5G array has been designed and evaluated in [11]. In order to increase the coverage of the phased mobile antenna array, two different methods have been introduced in [12] and [13]. In [12] the 3D coverage has been realized by switching between 3 sub-arrays mounted on a folded 3D structure. On the other hand, in [13] the 3D coverage has been achieved by using a surface wave in order to change radiation pattern main beam directions of the three planar sub-arrays. The bandwidth of the shown antennas is not so big and the wider bandwidth is wanted in order to achieve higher data rates. Furthermore, the exact operating frequency and bandwidth of the 5G communication system is still unknown. The phased mobile antenna array with wide scan angle has been proposed in [14]. However, the antenna does not have a large bandwidth. The bow-tie phased antenna array in [15] has a wide bandwidth and wide scan angle. Yet, designs in [14] and [15] require at least 6 mm clearance and only simulation results have been presented. The feeding network and connectors have not been implemented in these designs.

In this paper a quad-mode planar antenna with -10 dB bandwidth of 8.2 GHz and -6 dB bandwidth of 10.8 GHz with the clearance of 1.2 mm is proposed for the 5G mobile terminals. The wide bandwidth and wide scan angle is obtained by combining four modes. The wide embedded radiation patterns are achieved for the all four modes. Because of the wide embedded radiation patterns of array elements, the wide scan angle is achieved by the proposed array. In this paper, the coaxial to differential stripline transition is used to differentially feed the proposed array elements without a balun structure. In the final design the endfire radiation pattern has been obtained along the full operating frequency range of the array. In this paper, the endfire and broadside directions are defined as the directions along and perpendicular to the phone chassis, respectively. The final design is simulated in CST Microwave Studio and measured in the anechoic chamber.

In section II the properties of the proposed antenna are discussed using a simplified feed. Then, in section III the antenna element's operation in a linear array is examined. Later in section IV the more complex feeding with the connector is introduced. Finally, in section V the performance of the proposed mobile 5G phased antenna array with connectors

will be verified through measurements and simulations.

II. Antenna Geometry and Principle of Operation

In this section, the antenna geometry and operation principle will be explained. The 3D figure of the antenna geometry is shown in Fig. 1(a). The substrate has been made transparent in order to expose the internal antenna structure. The antenna element consists of two dipole arms on each side of the PCB. The dipole arms are joined to the ground plane on each side of PCB and also the top dipole arm is connected to the bottom one by two vias, as shown in Fig. 1(b) and Fig. 1(c). Other vias are utilized in order to suppress the unwanted surface wave. The notch, located between the two dipole arms, is used for impedance matching of the antenna. The Rogers RO3003 substrate with the height of 1.524 mm, relative permittivity of 3 and loss tangent of 0.001 has been used in the design. In a proposed setup, the antenna is fed between two vias by a discrete port on the top layer, as shown in Fig. 1.

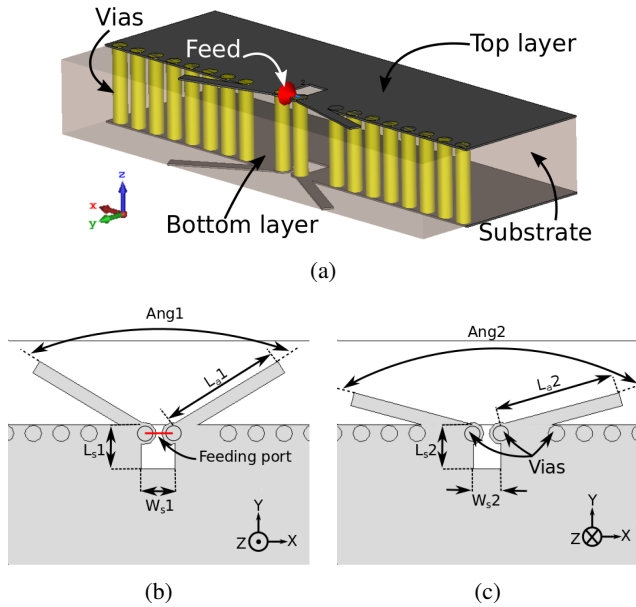

(a)

(b)   (c)

Fig. 1. (a) 3D view of the proposed antenna element, geometry of the proposed antenna in (b) top PCB view and (c) bottom PCB view.

When the antenna is excited, four distinctive modes are achieved. The sketch of the electric field produced by the each mode can be observed in Fig. 2. It can be noticed that modes 1 and 2 are generated by the dipole on the top PCB layer and modes 3 and 4 are generated by the dipoles on the bottom layer. When the antenna is resonating in the mode 1 and 3 the electric field is present between each of the dipole arms and the ground plane. When the antenna is resonating in mode 2 and 4 the electric field of dipole-like nature can be observed between the dipole arms in Fig. 2.

The reflection coefficient of the antenna and resonant frequencies of the modes are shown in Fig. 3(a). The reflection coefficient is plotted for the antenna with dimensions of: $Ang1 = 110°$ and $Ang2 = 140°$, lengths $L_a1 = L_a2 = 2.2$ mm, diameter of vias is 0.3 mm, the length of dipoles is 2.2 mm. Furthermore, the impedance of the antenna is plotted on smith

chart in Fig. 3(b). The impedance circles for all four modes can be observed at the resonant frequencies.

The resonant frequencies of the modes 1 and 2 depend on the length L_a1 and the resonant frequencies of the modes 3 and 4 are determined by the length L_a2. Furthermore, the resonant frequency of the modes are also affected by the angles $Ang1$ and $Ang2$. The Fig. 4(a) and Fig. 4(b) show parametric sweeps of angles from 100° to 160°. It can be seen that when Ang1 is changed, the resonances of modes 1 and 2 are affected. The Fig.4(b) shows that when the Ang2 is varied then the resonant frequencies of modes 3 and 4 are affected. However, the matching of modes 1 and 2 is affected as well.

The resonant frequencies of all the modes depend also on the height and dielectric constant of the substrate. The diameter of the two vias at the end of the dipole arms is also an important factor. The dimensions of the notch on the top layer and the bottom layer can be adjusted in order to change the antenna matching properties.

In order to obtain the desired performance of the antenna, the lengths L_a1 and L_a2 should be chosen to obtain two lower and two higher resonances. The position of resonances can be adjusted by changing angles Ang2 and Ang1. Ang2 is adjusted first, since it mainly changes mode 3,4 and affect mode 1 2. Next, adjust angle 1 since it mainly varies mode 1 2. Finally, the matching of modes can be fine tuned by altering the dimensions of the notches.
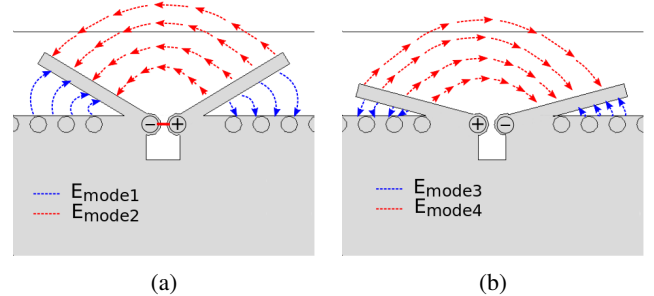

(a)   (b)

Fig. 2. Electric fields of the proposed antenna's modes in (a) top view and (b) bottom view.

The surface currents of the proposed antenna on the top copper plane are shown in Fig. 5 in order to get a better insight on the operating mechanism of the proposed antenna. It can be observed that the surface currents are strong for the mode 1 and 2 and weak for the mode 3 and 4 on the top copper plane. The surface currents spread along the edge for the mode 1 and concentrate close to the dipole and notch for the mode 2. The surface currents on the bottom copper plane for all modes are shown in Fig. 6. In this case, the reverse behavior can be observed: mode 3 and 4 have stronger surface currents than mode 1 and 2. In the way similar to the mode 1 and 2, mode 3 has strong surface currents along the edge of the ground plane and mode 4 have currents concentrated around the notch and dipole arms. From the Fig. 5 and Fig. 6 it can be concluded that the antenna on the top copper plane contributes to the radiation of modes 1 and 2 and the antenna on the bottom copper plane contributes to the radiation of modes 3 and 4.
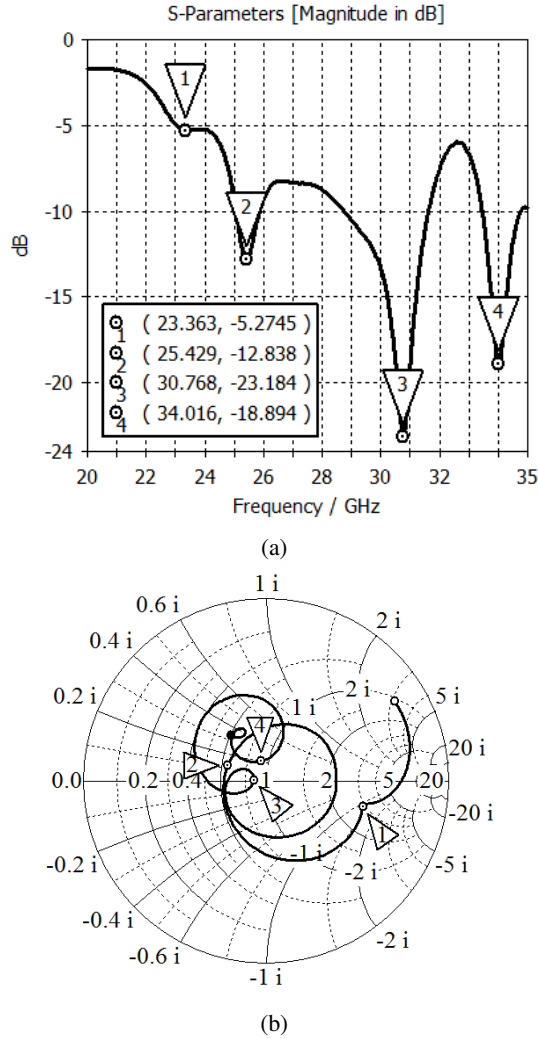
(a)

(b)

Fig. 3. (a) Reflection coefficient of the proposed antenna element, and (b) impedance of the proposed antenna plotted in Smith chart.

Furthermore, because the currents for the modes 1 and 3 are different from the surface currents of modes 2 and 4 it will be expected that those modes would have different radiation patterns when excited. The radiation patterns of a single antenna element are shown in Fig. 7 for all four modes. It can be clearly seen that radiation patterns of the modes 1 and 3 do not have a wanted end-fire radiation pattern. The two-lobe radiation pattern of modes 1 and 3 occurs because the E-field for those two modes concentrated between the dipole arms and the ground plane as shown in Fig. 2. However, the similar endfire radiation pattern is needed if the proposed antenna element should operate efficiently in an wideband array.

III. OPERATION IN AN ARRAY

In order to investigate the performance of the proposed element even further, a uniform linear array of 8 elements has been constructed on the short edge of the typical modern mobile phone ground plane, as shown in Fig. 8. In the application, the distance of 5.5 mm between elements has been chosen.

By introducing the neighboring elements, the open loop has been formed by the dipole arm of a neighboring element, the edge of the ground plane and one of the dipole arms of the

(a)

(b)

S1,1 (angle2=100°)   S1,1 (angle2=140°)
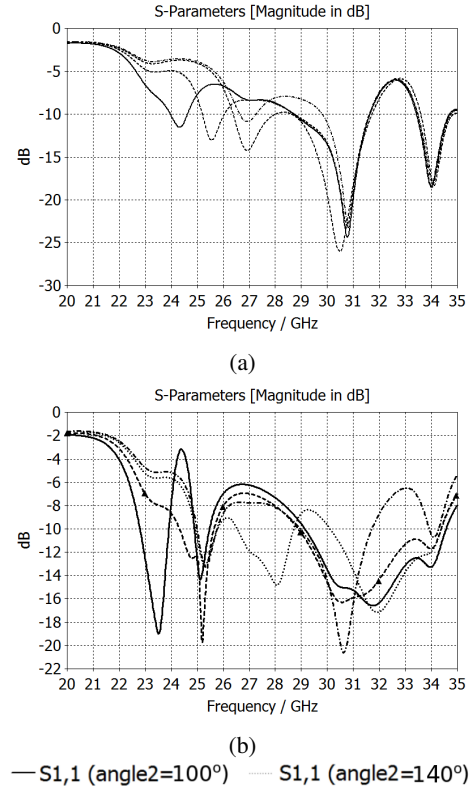S1,1 (angle2=120°)   S1,1 (angle2=160°)
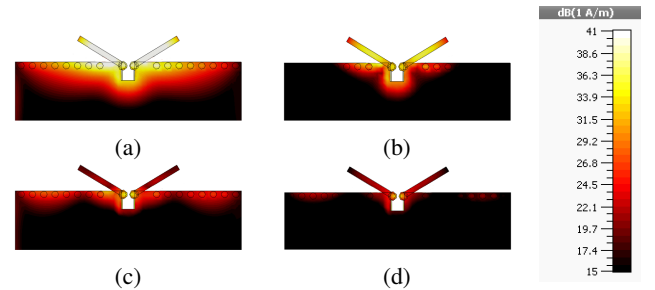
Fig. 4. Parametric sweep of (a) Ang1 and (b) Ang2.

Fig. 5. Surface currents on the top copper plane of the proposed antenna operating in (a) mode 1, (b) mode 2, (c) mode 3, and (d) mode 4.
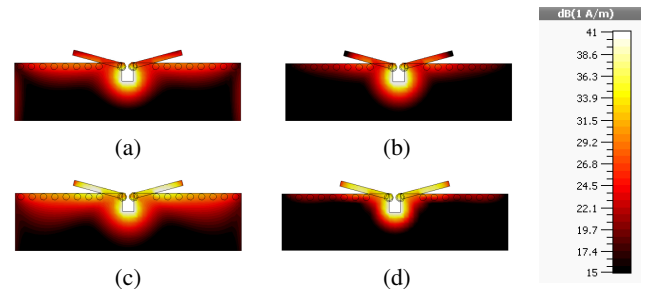

Fig. 6. Surface currents on the bottom copper plane of the proposed antenna operating in (a) mode 1, (b) mode 2, (c) mode 3, and (d) mode 4.

This article has been accepted for publication in a future issue of this journal, but has not been fully edited. Content may change prior to final publication. Citation information: DOI 10.1109/TAP.2018.2842303, IEEE Transactions on Antennas and Propagation
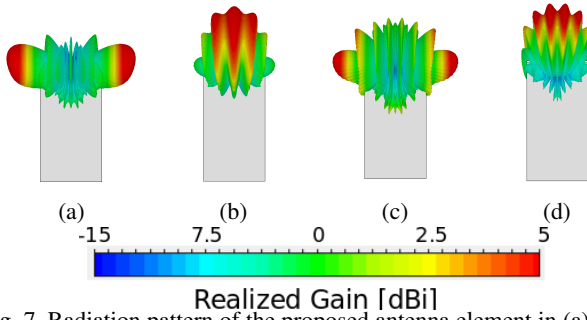
4

Fig. 7. Radiation pattern of the proposed antenna element in (a) mode 1, (b) mode 2, (c) mode 3, and (d) mode 4.

driven antenna. In Fig. 9 it is displayed how the surface currents will change when neighboring elements are introduced. This open loops help efficiently reduce the surface currents flowing on the ground for all four modes, and especially for modes 1 and 3. In this way, all the four modes will have similar current distributions and radiation patterns.
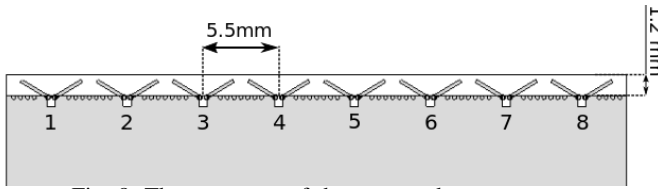

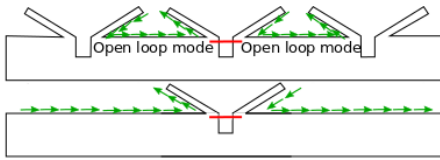Fig. 8. The geometry of the proposed antenna array.

Fig. 9. Sketch of the open loop formed by neighboring elements.

The surface currents of the proposed array element, located between two other elements, are shown on the top and bottom copper planes in Fig. 10 and Fig. 11, respectively. It can be clearly observed that the current distributions for four modes are similar, where the currents mainly concentrate around the driven element and two formed open loops. It is also noticed that the surface currents on the ground plane edge in mode 3 (see Fig. 11(c)) are relatively stronger than the other modes. Nonetheless, the mutual coupling between array elements is low and the isolation is always over 10 dB within the operating band.

The embedded radiation patterns of the proposed array element are shown in Fig. 12. It can be observed that when the proposed element operates in the array the endfire radiation pattern can be achieved in all of the modes. However, as expected from the corresponding surface currents, the radiation pattern for the mode 3 in Fig. 12(c) is not exactly endfire. Two sidelobes can be observed in Fig. 12(c), but the gain at the sidelobes is not that high in comparison to the main lobe. In addition, the inter-element spacing affects the sidelobe levels of the modes 1 and 3. And there is a compromise between the sidelobes of the modes 1 and 3.

It can clearly be seen that radiation patterns are not orthogonal anymore, as in the case in Fig. 7. Due to the open loops
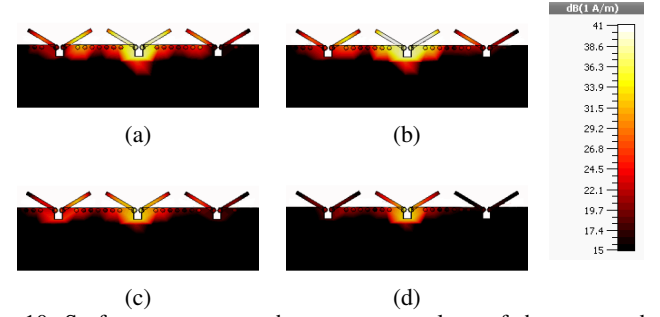
Fig. 10. Surface currents on the top copper plane of the proposed array element operating in (a) mode 1, (b) mode 2, (c) mode 3, and (d) mode 4.
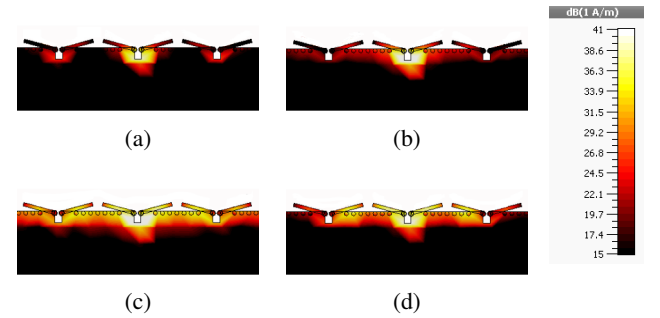
Fig. 11. Surface currents on the bottom copper plane of the proposed array element operating in (a) mode 1, (b) mode 2, (c) mode 3, and (d) mode 4.

formed by the neighboring elements and the ground plane in-between, the endfire radiation pattern are obtained for all the four modes.
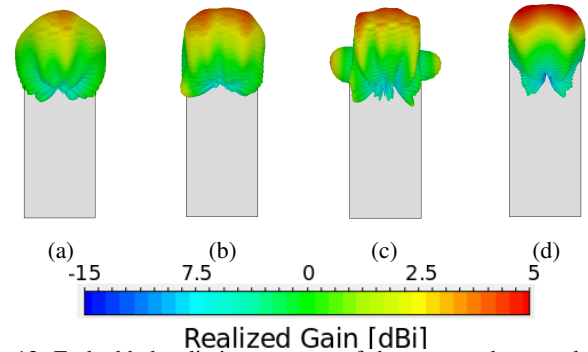
Fig. 12. Embedded radiation patterns of the proposed array element in (a) mode 1, (b) mode 2, (c) mode 3, and (d) mode 4.

Finally, the realized gain and sidelobe levels of the array are investigated for the different number of array elements. The isolation between elements is not shown because the metric of the realized gain already includes the coupling between array elements and return loss. The maximum realized gain of the array and sidelobe level are shown in Fig. 13 for array sizes from 2 to 8 elements. As expected, the realized gain increases and sidelobe level decreases with the number of elements. Yet, it can be seen that the difference between 7 and 8 element array is not significant. However, in the application the 8-element array has been chosen because the feeding network for the
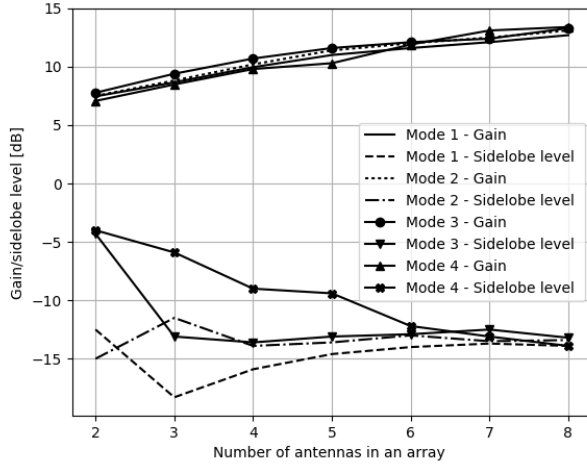
Fig. 13. Realized gain and sidelobe level of the proposed antenna array of different number of elements.

array of the odd number of elements is more challenging to make. Finally, one can notice that the difference of the curves for the maximum gain are within 1 dB for all of the modes.

IV. COAXIAL TO DIFFERENTIAL STRIPLINE TRANSITION

The proposed antenna has to be differentially driven as shown in Fig. 1. Usually, a Wilkinson power divider and a wideband 180° phase shifter are used to make a differential feeding. An example of this antenna feeding technique is shown in [16]. Another way to achieve the differential feeding is to use the 180° ring hybrid coupler. However, hybrid coupler structures are large in size and would significantly decrease the area available for the electronic components on the mobile phone ground plane. In this paper, it has been proposed to make a less complex coaxial to differential stripline transition in order to achieve the differential feeding of the antenna.

The overview of the antenna structure in 3D (where the substrate has been made transparent) and the internal feeding structure of the proposed antenna are shown in Fig 14. The differential stripline is connected to the two middle vias on the antenna structure. One of those vias is connected to the coaxial inner connector and the other is connected to the coaxial ground. The MMPX PCB CMD jack [17] (model number: $82_M MPX - S50 - 0 - 2$) has been mounted on the top ground plane. The PCB jack has been placed as close as possible to the antenna, in order to reduce the length and loss of the differential stripline.

The coaxial part of the connector extends all the way to the top ground plane. At the other end, the differential stripline has been connected to the top and bottom dipole antennas through the vias. Furthermore, now the antenna structure is more complex and requires at least one more additional layer for the differential stripline. Finally, the surface wave suppression vias have been added around the feeding structure. The exploded view of the connector and feeding structure is shown in Fig. 14(c).

The micro-via connected to the inner connector (center conductor) of the coaxial cable and one of the striplines.

The through via connects the both ground planes, an outer-connector of the coaxial cable and the other stripline together. By using the proposed structure a balun is not required in order to achieve differential feeding of the antenna.

(a)   (b)

(c)
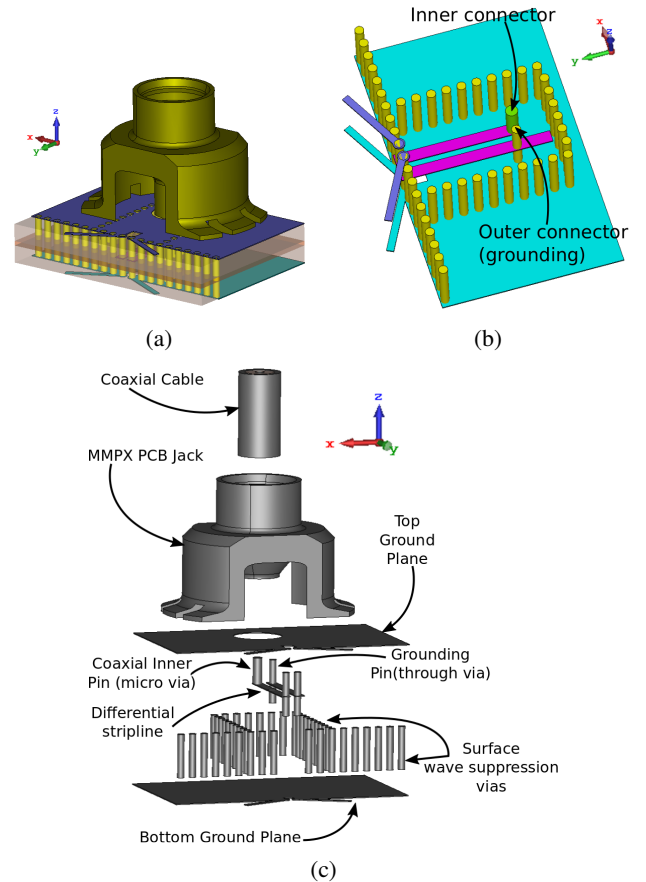
Fig. 14. (a) 3D view of the antenna with the MMPX connector and feeding structure and (b) view of the internal feeding structure, and (c) Exploded view of the connector and feeding structure.

V. PHASED ARRAY WITH CONNECTORS

In this section a final phased array design, consisting of the 8 antennas with 8 MMPX connectors, is presented. The proposed phased antenna array performance is verified by the simulations in the CST Microwave Studio with more than 35.7 million FDTD mesh cells. The smallest cell size is 0.037 345 7 mm and largest cell size is 0.746 58 mm. Furthermore, the prototype of the array is constructed and measured in the anechoic chamber.

A. Geometry

The proposed phased antenna array has been made on the four copper layers. Two Taconic RF-30 ($\varepsilon_r = 3$, $\tan(\delta) = 0.0014$) 0.762 mm substrates have been glued with FR-4 ($\varepsilon_r = 4.3$, $\tan(\delta) = 0.025$) glue with 0.2 mm thickness. However, the FR4 glue does not affects the performance of the antenna significantly. The overview of the layers used in the antenna array PCB construction is shown in Fig. 15(a). The full PCB layout is shown in Fig. 15(b) and Fig. 15(c), consisting of four layers, vias and microvias. Because of the connector physical

dimension limitations, it has been chosen to mount connectors both on the top and bottom layers. It can be seen that a mixture of micro-vias and vias has been used. The layer 2 is separated from the layer 3 by the 0.2 mm thick FR-4 glue.

(a)

(b)

(c)

Fig. 15. Overview of the layers in the antenna structure (a) Overview of the PCB layers, (b) layer 1 and 2, and (c) layer 3 and 4.
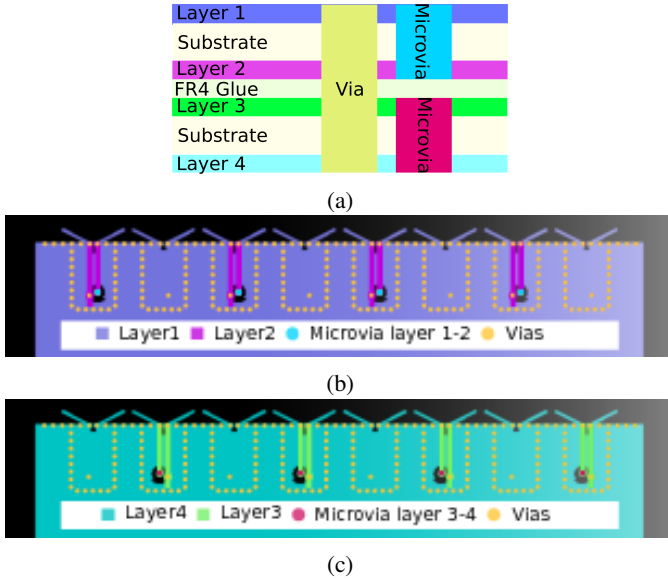
The top and side views of the phased antenna array are shown in Fig. 16. Only the top the PCB has been shown because the bottom of the PCB looks exactly the same as the top. The dimensions of the ground plane are 106×47.5 mm. The clearance is only 1.2 mm, as shown in Fig. 16. The side view of the PCB is shown in Fig. 16(b) where connectors mounted on the both sides of the PCB can be spotted. Furthermore, the Taconic RF-30 layers are displayed in the light blue. The dimensions of the array element has been altered in respect to the Fig. 1 because the feeding point has been moved, and also the ground plane thickness has been increased (FR4 glue has been added). The final antenna element has following dimensions:

- Dipole length $L_a1 = L_a2 = 2.4$ mm
- Angle between the dipole arms $Ant1 = Ang2 = 63°$
- $L_s1 = 0.9$ mm
- $L_s2 = 0.6$ mm
- $W_s1 = 0.5$ mm
- $W_s2 = 0.4$ mm
- Width of the dipole arms $= 0.2$ mm
- Diameter of vias is 0.3 mm
- Distance between vias is 0.4 mm
- Microvia diameter is 0.4 mm
- Stripline width is 0.4 mm
- Distance between striplines is 0.21 mm
- Thickness of all copper planes is 0.034 mm

B. Measurement Procedure

Next, the phased antenna array prototype and measurement setup are shown in Fig. 17. The zoomed in view of the connectors and antennas can be seen in Fig. 17(a). However, the
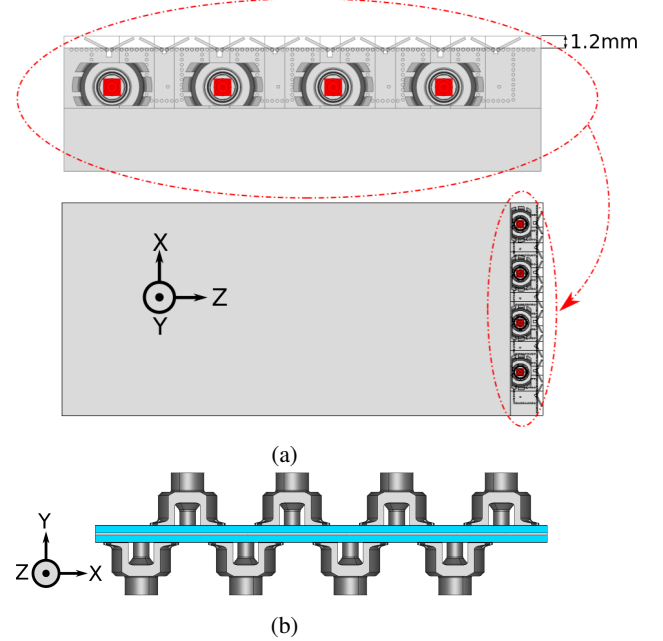

(a)

(b)

Fig. 16. Geometry of the phased antenna array with connectors (a) top view and (b) side view.

solder has not been included in the simulations. The coordinate system can be seen in Fig. 17(b). In measurement only one antenna has been measured at a time, and 20 dB attenuators have been connected to the two neighboring elements. The available measurement system can only measure up to 140° in the elevation plane. Thus, it has been chosen to orient antenna in such a way, so the maximum gain is measured in $\theta = 0°$ direction. Furthermore, the system has better resolution at the top and worse resolution at the sides ($\theta = 90°$ plane). The 5° resolution has been chosen both in the elevation and azimuth planes.

Typically, it is very challenging to measure the phase of the antenna radiation pattern accurately in the anechoic chamber. On the other hand, the magnitude of the radiation pattern can be obtained by comparing it to the known antenna (a standard gain horn has been used here). In order to measure the phase accurately the phase center of the measurement system should be found and located first. In this measurement, the phase center has been located by using a simple monopole antenna and a probe horn. The monopole antenna is rotated and the 2D radiation pattern is measured by the probe horn. The phase of the monopole antenna is constant when the antenna is located in the phase center of the measurement system.

After locating the system phase center, there are two ways of measuring the antenna array accurately. The first way is to put the antenna array center at the phase center of a measuring system and do not move the array location while all the elements are measured. The second way is to move each measured antenna element to the phase center of a measurement system each time when the measurement is performed.

If the phase center is fixed to each array element, then the gain of phased array can be computed as:

This article has been accepted for publication in a future issue of this journal, but has not been fully edited. Content may change prior to final publication. Citation information: DOI 10.1109/TAP.2018.2842303, IEEE Transactions on Antennas and Propagation

7

$$G_{array} = G_1 \cdot e^{j(k \cdot d \cdot sin(\theta)+\beta_1)} + G_2 \cdot e^{j(k \cdot d \cdot sin(\theta)+\beta_2)} + \quad (1)$$
$$... + G_8 \cdot e^{j(k \cdot d \cdot sin(\theta)+\beta_8)}$$

where:

- $G_1...G_8$ is a measured gain pattern of each antenna element.
- $k = \frac{2\pi}{\lambda}$ is a wave number.
- θ is the angle between the array scanning direction and the boresight direction.
- $\beta_1...\beta_8$ is a phase shift at each element's feed.

However, if the phase center is fixed with respect to the whole array, then the term $k \cdot d \cdot sin(\theta)$ is already included in the measurement. Thus the Eq.1 can be reduced to the following form:

$$G_{array} = G_1 \cdot e^{j \cdot \beta_1} + G_2 \cdot e^{j \cdot \beta_2} + ... + G_8 \cdot e^{j \cdot \beta_8} \quad (2)$$

Theoretically both methods are equally accurate for obtaining the correct radiation pattern phase. However, if the exact location of array element's phase center is not known, then the first method will be more accurate.

Finally, when processing the results it is important to mention that the pattern of each element should be calibrated at the boresight. In order to perform the beamforming correctly, the phase of each element at the boresight should have the same value. Furthermore, the phase calibration at the boresight should be done for co-polarized measurement, because the phase is more correct if the gain of antenna is high. In this paper the first measurement method has been applied.
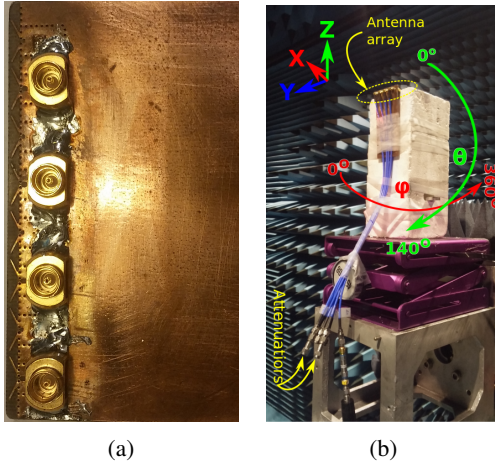

Fig. 17. Prototype of the phased antenna array with connectors (a) zoomed in and (b) suspended in the anechoic chamber.

C. S-parameters

The simulated and measured reflection coefficients of the phased antenna array are shown in Fig. 18. It can be noticed that the four resonances, shown in Fig. 3(a), cannot be observed anymore because the geometry of the antenna has been changed. Furthermore, the parasitic resonance at the frequencies lower than 24 GHz can be observed both in simulations and measurements. Only 7 antennas have been

measured because the antenna number 8 on the edge was not working because of the prototype production error. However, it can clearly be seen that simulations and measurements agree quite well. Only, the region around 30 GHz has around −6 dB matching, which is an acceptable value for a mobile antenna.
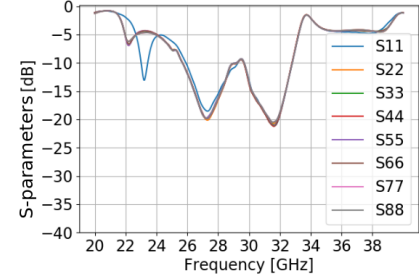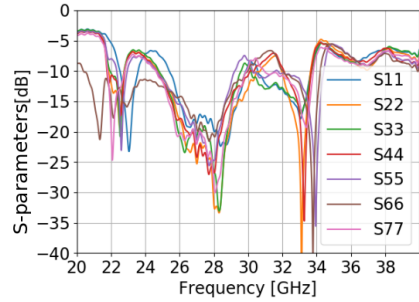
Fig. 18. Embedded reflection coefficients of (a) simulated array and (b) measured array.

D. Scan Angle

To investigate the scanning performance of the phased antenna array it has been chosen to look on the scan angle. In order to illustrate the scan angle, the main beam of the phased antenna array has been shown in the scanning range from -90° to 90° in Fig. 19. Notice that in order to form the array, the radiation pattern of the broken antenna element number 8 has been obtained by mirroring the radiation pattern of the element number 1. This can be done because of the antenna array symmetry around Z-axis. Furthermore, because connectors are mounted on the both sides of PCB, in post-processing the phase of every second antenna should be altered 180° in order to execute the beamforming correctly. Because in the final design the four modes could not be distinguished it has been chosen to illustrate the scanning results for the frequencies of 25, 27, 29, 31, and 33 GHz. Nonetheless, the measurements have been carried out in the frequency band from 25 to 33 GHz.

Wide scan angle behavior of the phased array can be observed in both simulations and measurements. However, the gain of the measured radiation patterns is higher when array is scanned to the large scan angles. Furthermore, the position of the beams for each scan angle in simulations and measurements are similar, which means that the prototype has correct dimensions and distance between elements. The

beamforming pattern in Fig. 19(a) is more peaky than measurements in Fig. 19(b). It can also be observed that in Fig. 19(h) the maximum gain is 2 dB lower than that in simulations in Fig. 19(g). In Fig. 19(e) the simulated gain is approximately 2 dB lower than measured in Fig. 19(f).

The scan angle of the proposed phased antenna array is comparable to the other proposed mobile phased array designs. In [12] a switchable antenna array with the scan angle of around ±80° has been proposed. In [13] a slot antenna array with the scan angle of ±70° has been designed. Then, in [9] a low profile antenna has been proposed with the scan angle of ±80°. Finally, in [14] the wide scan antenna array with the scan angle of over ±85° has been proposed. However, all of those phased array designs have a narrow band characteristics or require big clearance to achieve wide scan angles.

E. Total Scan Pattern

In order to investigate the coverage of the phased antenna array, the total scan pattern (TSP) has been calculated. The total scan pattern is a combination of all possible phased antenna array's scan angles, where the best possible gain has been chosen at each spatial point. Progressive phase shifts of -180 to 180° have been applied to the antenna elements both in measurements and simulations. It has been chosen to show the TSP in the θ ranges from 0 to 140° both for measurements and simulations in order to reach the fair comparison.

The TSPs for the 25, 27, 29, 31 and 33 GHz frequencies are plotted in Fig. 20. First, it can be noticed that the maximum gain is higher for the measured array prototype. Also, the measured TSP of the prototype is not uniform because of the probable reflections in the anechoic chamber. Then again, the shapes of the total scan patterns for the simulations and measurements look similar.

F. Coverage Efficiency

Importantly, in order to have a full picture of the proposed phased antenna array performance the coverage efficiency has been calculated for the frequencies from 25 to 33 GHz. The coverage efficiency described the spatial coverage of the phased antenna array system and defined as [7]:

$$\eta_c = \frac{\text{Coverage Solid Angle}}{\text{Maximum Solid Angle}} \quad (3)$$

where maximum solid angle defined as 4π steradians.

The curves for the simulated and measured coverage efficiency are shown in Fig. 21. The lowest coverage can be observed at 30 GHz both in simulations and measurements. However, the measured coverage efficiency at 30 GHz, especially in the high gain region ($\geq$ 7 dBi), is lower than the simulated. The highest achievable simulated coverage occurs at 27 and 28 GHz. Having said that, the measured coverage at 25 GHz is also very high.

Finally, the mean and variance values of the coverage efficiency have been calculated from all frequency curves in Fig. 21. The simulated and measured mean coverage efficiency have very similar coverage values down to 2.5 dBi of threshold gain. The 50 % coverage with the gain of 5 dBi has been

Fig. 19. 2D scan of the proposed phased antenna array (a) simulations at 25 GHz, (b) measurements at 25 GHz, (c) simulations at 27 GHz, (d) measurements at 27 GHz, (e) simulations at 29 GHz, (f) measurements at 29 GHz, (g) simulations at 31 GHz, (h) measurements at 31 GHz, (i) simulations at 33 GHz, and (j) measurements at 33 GHz.

achieved. It means that if another proposed array is placed on the opposite edge of the ground plane and then the coverage efficiency of 100 % would be achieved with the gain of 5 dBi. The measured coverage efficiency has as much as 0.5 % more variance at the gain of 5 dBi in Fig. 22(b). These variance values can be explained by the unwanted reflections are present in the anechoic chamber under the measurement. The variance is lower towards the very low and very high gains.

VI. Conclusion

In this paper, a quad-mode endfire planar phased 5G mobile antenna array with large scan angle and extremely small

This article has been accepted for publication in a future issue of this journal, but has not been fully edited. Content may change prior to final publication. Citation information: DOI 10.1109/TAP.2018.2842303, IEEE Transactions on Antennas and Propagation

9

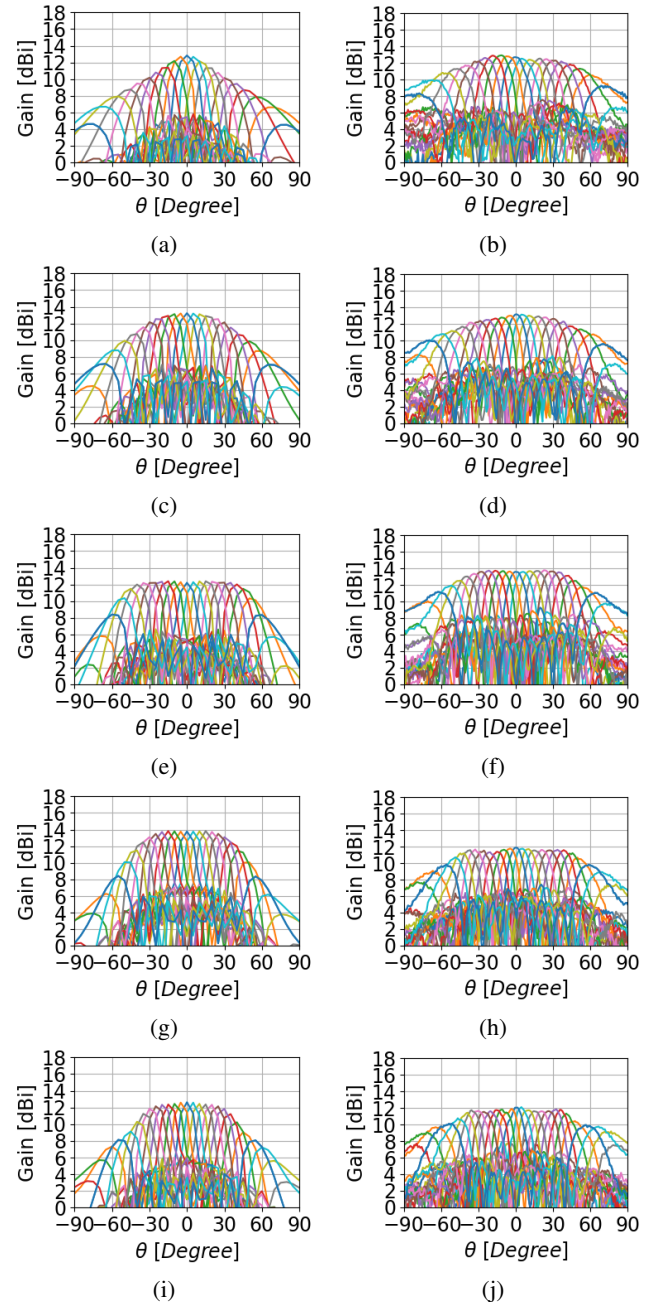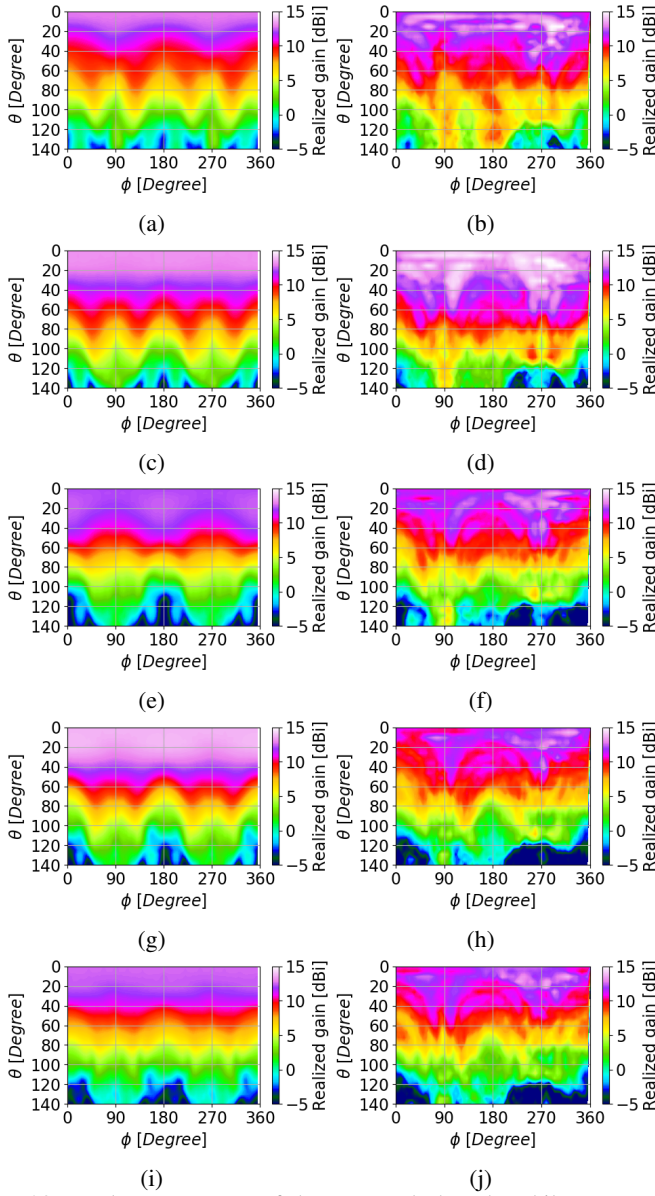Fig. 20. Total scan patterns of the proposed phased mobile antenna array (a) simulations at 25 GHz, (b) measurements at 25 GHz, (c) simulations at 27 GHz, (d) measurements at 27 GHz, (e) simulations at 29 GHz, (f) measurements at 29 GHz, (g) simulations at 31 GHz, (h) measurements at 31 GHz, (i) simulations at 33 GHz, (j) measurements at 33 GHz.

Fig. 21. Coverage efficiency of the phased antenna array: (a) simulations and (b) measurements.
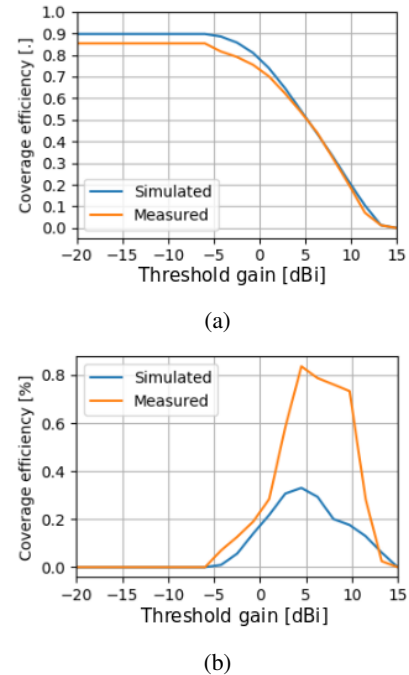
Fig. 22. Statistical investigation of measured and simulated coverage efficiency: (a) mean and (b) variance.

clearance has been proposed. The array element designed in this paper has different radiation patterns for each mode, but when combined into a linear array the embedded radiation patterns of an element are similar. The optimal distance between elements should be chosen in order to obtain the clean endfire embedded radiation patterns for the array elements in all modes. Furthermore, it has been shown how the surface currents and radiation patterns of an element change when combined into an array.

In order to make the proposed element design more practical for the mobile terminal applications, it has been chosen to used MMPX connectors and a feeding structure. Here it has been proposed to use coaxial to differential stripline feeding transition. Then a four-layer PCB has first been simulated in CST Microwave Studio and then measured in the anechoic
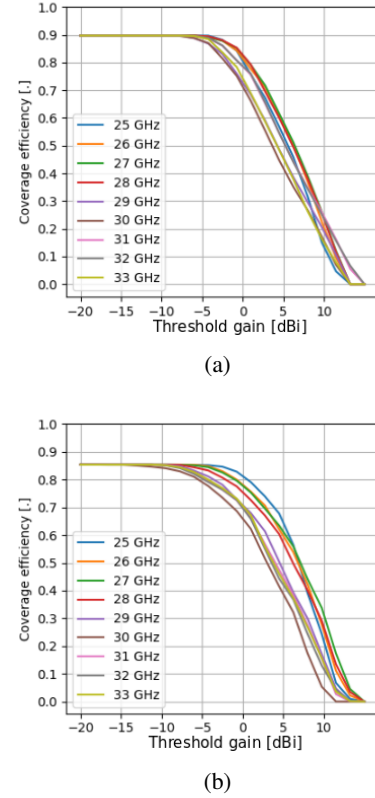
This article has been accepted for publication in a future issue of this journal, but has not been fully edited. Content may change prior to final publication. Citation information: DOI 10.1109/TAP.2018.2842303, IEEE Transactions on Antennas and Propagation

10

chamber. The final phased antenna array design has a scan angle of over 140° and impedance bandwidth of 8 GHz.

Finally, the total scan pattern and coverage efficiency of the measured and simulated phased array antenna have been calculated in the range from 25 to 33 GHz. The total scan patterns have the similar shapes for simulations and measurements. The mean coverage efficiency along the frequency range is very similar in measurements and simulations, but the measured antenna array has slightly more variance in the coverage efficiency between the frequency points. The coverage efficiency of around 50 % with the gain of 5 dBi has been achieved on average in the chosen frequency range.

REFERENCES

[1] T. S. Rappaport, S. Sun, R. Mayzus, H. Zhao, Y. Azar, K. Wang, G. N. Wong, J. K. Schulz, M. Samimi, and F. Gutierrez, "Millimeter Wave Mobile Communications for 5G Cellular: It Will Work!," *IEEE Access*, vol. 1, pp. 335–349, 2013.

[2] W. Roh, J. Y. Seol, J. Park, B. Lee, J. Lee, Y. Kim, J. Cho, K. Cheun, and F. Aryanfar, "Millimeter-wave beamforming as an enabling technology for 5G cellular communications: theoretical feasibility and prototype results," *IEEE Commun. Mag.*, vol. 52, pp. 106–113, Feb. 2014.

[3] S. J. Nawaz, N. M. Khan, M. N. Patwary, and M. Moniri, "Effect of Directional Antenna on the Doppler Spectrum in 3-D Mobile Radio Propagation Environment," *IEEE Trans. Veh. Technol.*, vol. 60, no. 7, pp. 2895–2903, 2011.

[4] T. Manabe, Y. Miura, and T. Ihara, "Effects of antenna directivity and polarization on indoor multipath propagation characteristics at 60 GHz," *IEEE Journal on Selected Areas in Communications*, vol. 14, pp. 441–448, Apr. 1996.

[5] Y. Azar, G. N. Wong, K. Wang, R. Mayzus, J. K. Schulz, H. Zhao, F. Gutierrez, D. Hwang, and T. S. Rappaport, "28 GHz propagation measurements for outdoor cellular communications using steerable beam antennas in New York city," *2013 IEEE International Conference on Communications (ICC)*, pp. 5143–5147, 2013.

[6] M. U. Rehman, X. Chen, C. G. Parini, and Z. Ying, "Evaluation of a statistical model for the characterization of multipath affecting mobile terminal GPS antennas in sub-urban areas," *IEEE Trans. Antennas Propag.*, vol. 60, pp. 1084–1094, Feb. 2012.

[7] J. Helander, K. Zhao, Z. Ying, and D. Sjöberg, "Performance analysis of millimeter-wave phased array antennas in cellular handsets," *IEEE Antenna Wireless Propag. Lett.*, vol. 15, pp. 504–507, 2016.

[8] W. Hong, S. T. Ko, Y. Lee, and K. H. Baek, "Multi-polarized antenna array configuration for mmWave 5G mobile terminals," *2015 International Workshop on Antenna Technology (iWAT)*, pp. 60–61, Mar. 2015.

[9] W. Hong, K. Baek, Y. Lee, and Y. G. Kim, "Design and analysis of a low-profile 28 GHz beam steering antenna solution for Future 5G cellular applications," *Microwave Symposium (IMS), 2014 IEEE MTT-S International*, pp. 1–4, Jun. 2014.

[10] N. Ojaroudiparchin, M. Shen, and G. F. Pedersen, "Design of Vivaldi antenna array with end-fire beam steering function for 5G mobile terminals," *2015 23rd Telecommunications Forum Telfor (TELFOR)*, pp. 587–590, 2015.

[11] R. Hussain, A. T. Alreshaid, S. K. Podilchak, and M. S. Sharawi, "Compact 4G MIMO antenna integrated with a 5G array for current and future mobile handsets," *IET Microwaves, Antennas & Propagation*, vol. 11, no. 2, pp. 271–279, 2017.

[12] N. Ojaroudiparchin, M. Shen, S. Zhang, and G. F. Pedersen, "A Switchable 3-D-Coverage-Phased Array Antenna Package for 5G Mobile Terminals," *IEEE Antennas Wireless Propag. Lett.*, vol. 15, pp. 1747–1750, 2016.

[13] S. Zhang, X. Chen, I. Syrytsin, and G. F. Pedersen, "A Planar Switchable 3D-Coverage Phased Array Antenna and Its User Effects for 28 GHz Mobile Terminal Applications," *IEEE Trans. Antennas Propag.*, vol. 65, pp. 6413–6421, Dec. 2017.

[14] N. Ojaroudiparchin, M. Shen, and G. F. Pedersen, "Wide-scan phased array antenna fed by coax-to-microstriplines for 5G cell phones," *2016 21st International Conference on Microwave, Radar and Wireless Communications (MIKON)*, pp. 1–4, 2016.

[15] N. O. Parchin, M. Shen, and G. F. Pedersen, "End-fire phased array 5G antenna design using leaf-shaped bow-tie elements for 28/38 GHz MIMO applications," *2016 IEEE International Conference on Ubiquitous Wireless Broadband (ICUWB)*, pp. 1–4, 2016.

[16] M. Z. Azad and M. Ali, "Novel wideband directional dipole antenna on a mushroom like ebg structure," *IEEE Trans. Antennas Propag.*, vol. 56, pp. 1242–1250, May 2008.

[17] Huber+Suhner, "MMPX 67 GHz /80 Gbps Snap-on Connectors." http://pdf.directindustry.com/pdf/huber-suhner/mmpx-connectors/30583-293349.html.

Igor Syrytsin was born in Saratov, Russia, in 1988. He received the B.S. degree in electronic engineering and IT and M.S. degree in wireless communication systems from Aalborg University, Aalborg, Denmark, in 2014 and 2016, respectively. Currently, he is pursuing the Ph.D. degree at Department of Electronic Systems at Aalborg University. His research interests include mm-wave mobile antenna design and interactions between user and mobile antennas.

Shaui Zhang received the B.E. degree from the University of Electronic Science and Technology of China, Chengdu, China, in 2007 and the Ph.D. degree in electromagnetic engineering from the Royal Institute of Technology (KTH), Stockholm, Sweden, in 2013. After his Ph.D. studies, he was a Research Fellow at KTH. In April 2014, he joined Aalborg University, Denmark, where he currently works as Associate Professor. In 2010 and 2011, he was a Visiting Researcher at Lund University, Sweden and at Sony Mobile Communications AB, Sweden, respectively. He was also an external antenna specialist at Bang & Olufsen, Denmark from 2016-2017. He has coauthored over 40 articles in well-reputed international journals and over 14 (US or WO) patents. His research interests include: mobile terminal mm-wave antennas, biological effects, CubeSat antennas, UWB wind turbine blade deflection sensing, MIMO antenna systems, and RFID antennas.

This article has been accepted for publication in a future issue of this journal, but has not been fully edited. Content may change prior to final publication. Citation information: DOI 10.1109/TAP.2018.2842303, IEEE Transactions on Antennas and Propagation

11

Gert Frølund Pedersen was born in 1965. He received the B.Sc. and E.E. (Hons.) degrees in electrical engineering from the College of Technology in Dublin, Dublin Institute of Technology, Dublin, Ireland, in 1991, and the M.Sc.E.E. and Ph.D. degrees from Aalborg University, Aalborg, Denmark, in 1993 and 2003, respectively. Since 1993, he has been with Aalborg University where he is a Full Professor heading the Antenna, Propagation and Networking LAB with 36 researchers. He is also the Head of the Doctoral School on wireless communication with some 100 Ph.D. students enrolled. His research interests include radio communication for mobile terminals especially small antennas, diversity systems, propagation, and biological effects. He has published more than 175 peer reviewed papers and holds 28 patents. He has also worked as a Consultant for developments of more than 100 antennas for mobile terminals including the first internal antenna for mobile phones in 1994 with lowest SAR, first internal triple-band antenna in 1998 with low SAR and high TRP and TIS, and lately various multiantenna systems rated as the most efficient on the market. He has worked most of the time with joint university and industry projects and have received more than 12 M$ in direct research funding. He is currently the Project Leader of the SAFE project with a total budget of 8 M$ investigating tunable front end including tunable antennas for the future multiband mobile phones. He has been one of the pioneers in establishing over-the-air measurement systems. The measurement technique is now well established for mobile terminals with single antennas and he was chairing the various COST groups (swg2.2 of COST 259, 273, 2100, and now ICT1004) with liaison to 3GPP for over-the-air test of MIMO terminals. He is currently involved in MIMO OTA measurement.

Arthur S. Morris III (S'90–M'91–SM'04–F'13) received the B.S. degree in physics and also in electrical engineering and M.S. and Ph.D. degrees in electrical engineering from North Carolina State University (NCSU), Raleigh, NC, USA, in 1983, 1986, and 1993, respectively. As a Scientist/Engineer with a concentration on physical electronics and electromagnetic fields for over 30 years, he has contributed to device technologies ranging from traveling-wave tubes to millimeter-wave heterojunction bipolar transistors and has developed products for markets from high-voltage instrumentation to broadband communication systems. In 1999, he joined Coventor, to lead software and hardware development to drive the transition of microelectromechanical systems (MEMS) and microsystems from the laboratory into products for RF and optical applications. He is a cofounder of Wispry Inc., Irvine, CA, USA, which spun out of Coventor in 2002. He is the company's Chief Technical Officer (CTO) and leads the development of high-performance programmable RF products for high-volume markets utilizing MEMS, CMOS, and advanced packaging. He is an Adjunct Professor with NCSU.